Naval Research Laboratory

Washington, DC 20375-5320

NRL/MR/7322--20-10,051

Deconvolution of Satellite-Based Passive Microwave Brightness Temperatures Using Visible/Infrared Observations

Li Li
Elizabeth Twarog

Remote Sensing Physics Branch
Remote Sensing Division

David Truesdale

Johns Hopkins University Applied Physics Laboratory
Laurel, Maryland

Jeffrey Bowles
Gia Lamela
Bo-Cai Gao

Coastal and Ocean Remote Sensing Branch
Remote Sensing Division

June 25, 2020

REPORT DOCUMENTATION PAGE

Form Approved
OMB No. 0704-0188

1. REPORT DATE *(DD-MM-YYYY)* 25-06-2020	**2. REPORT TYPE** NRL Memorandum Report	**3. DATES COVERED** *(From - To)* 1 Oct 2014 – 30 Sept 2019

4. TITLE AND SUBTITLE

Deconvolution of Satellite-Based Passive Microwave Brightness Temperatures Using Visible/Infrared Observations

5a. CONTRACT NUMBER

5b. GRANT NUMBER

5c. PROGRAM ELEMENT NUMBER

6. AUTHOR(S)

Li Li, David Truesdale*, Jeffrey Bowles, Gia Lamela, Bo-Cal Gao, and Elizabeth Twarog

5d. PROJECT NUMBER

5e. TASK NUMBER

5f. WORK UNIT NUMBER
6769, 6A49

7. PERFORMING ORGANIZATION NAME(S) AND ADDRESS(ES)

Naval Research Laboratory
4555 Overlook Avenue, SW
Washington, DC 20375-5320

8. PERFORMING ORGANIZATION REPORT NUMBER

NRL/MR/7223--20-10,051

9. SPONSORING / MONITORING AGENCY NAME(S) AND ADDRESS(ES)

Naval Research Laboratory
4555 Overlook Avenue, SW
Washington, DC 20375-5320

10. SPONSOR / MONITOR'S ACRONYM(S)

11. SPONSOR / MONITOR'S REPORT NUMBER(S)

12. DISTRIBUTION / AVAILABILITY STATEMENT

DISTRIBUTION STATEMENT A: Approved for public release; distribution is unlimited.

13. SUPPLEMENTARY NOTES

*Johns Hopkins University Applied Physics Laboratory, 11100 Johns Hopkins Road, Laurel, Maryland 20723-6099

14. ABSTRACT

This paper details a technique for deconvolving satellite microwave radiometer brightness temperatures into component passive microwave emissions from water and land. This process utilizes high resolution visible and infrared satellite observations from the Aqua and Terra MODIS spectro-radiometers to generate antenna gain pattern corrected fractional weights for water coverage within each radiometer field of view. Our results comparing component brightness temperatures generated from in situ and simulated data to deconvolved component and observed brightness temperatures indicate a significant decrease in the bias and root mean squared error of land based passive microwave emissions.

15. SUBJECT TERMS

16. SECURITY CLASSIFICATION OF:			**17. LIMITATION OF ABSTRACT**	**18. NUMBER OF PAGES**	**19a. NAME OF RESPONSIBLE PERSON** Elizabeth Twarog
a. REPORT Unclassified Unlimited	**b. ABSTRACT** Unclassified Unlimited	**c. THIS PAGE** Unclassified Unlimited	Unclassified Unlimited	24	**19b. TELEPHONE NUMBER** *(include area code)* (202) 767-9130

This page intentionally left blank.

CONTENTS

This page intentionally left blank.

EXECUTIVE SUMMARY

This report details a technique for deconvolving satellite microwave radiometer brightness temperatures into component passive microwave emissions from water and land surfaces. This process utilizes high resolution visible and infrared satellite observations from the Aqua and Terra MODIS spectro-radiometers to generate antenna gain pattern corrected fractional weights for water coverage within each radiometer field of view. We then use multiple overlapping brightness temperature observations to construct a system of linear equations, which we solve through least squares minimization. Our results comparing component brightness temperatures generated from *in situ* and simulated data to deconvolved component and observed brightness temperatures indicate a significant decrease in the bias and root mean squared error of land based passive microwave emissions.

This page intentionally left blank.

DECONVOLUTION OF SATELLITE-BASED PASSIVE MICROWAVE BRIGHTNESS TEMPERATURES USING VISIBLE/INFRARE OBSERVATIONS

1. INTRODUCTION

Remote sensing of soil moisture via satellite radiometers has made great strides in recent years. Radiometers designed to measure soil moisture such as those aboard NASA's Soil Moisture and Ocean Salinity (SMOS) [1] and Soil Moisture Active Passive (SMAP) [2] missions as well as general radiometers such as AMSR-E, AMSR2 and WindSat [3,4] are now producing accurate global soil moisture retrievals with short (1 - 3 day) revisit times. However, these soil moisture products still suffer from significant limitations in areas containing large water bodies. A single satellite observation containing significant surface water has to be discarded in soil moisture retrievals. This report details a method for utilizing satellite-based visible and infrared (Vis/IR) observations to deconvolve the land based passive microwave (passive microwave) contributions from those emitted by water in these mixed pixel cases; thus enabling soil moisture retrievals in these areas.

A similar technique was developed by Bellerby et al. [5] to separate land and sea component T_B s for the 37 GHz channel on the Special Sensor Microwave Imager (SSM/I) on the United States Defense Meteorological Satellite Program (DMSP) series of spacecrafts. Their technique used a similar antenna pattern and spatial over-sampling based deconvolution process, but they relied on digital coastal maps to provide their land-to-water ratio weighting. By using concurrent Vis/IR observations, we hope that the technique presented here proves more extensible into deconvolution of bare soil, vegetation, snow, mountainous terrain, etc. Additionally, a version of passive microwave brightness temperature (T_B) deconvolution has been demonstrated with data from the Passive and Active L and S band radiometer (PALS) from the SMEX02 field campaign in Iowa [6], though our approach differs significantly from theirs. Our approach is also similar to deconvolution methods used for spatial resolution enhancement [7,8], but here we are using oversampling to separate component T_Bs from different emission sources within a radiometer's field of view (FOV) rather than separate T_B emissions from spatial subpixels.

Our technique begins by using Vis/IR data from NASA's Moderate Resolution Imaging Spectrometer (MODIS) instruments [9] to produce 1 km spatial resolution maps of fractional water coverage within each MODIS grid pixel. We then convolve these fractional coverages according to the passive microwave radiometer's antenna gain pattern to determine the relative contribution weights within the radiometer's FOV for passive microwave emissions from both water and land surfaces. These weights, together with those from adjoining FOVs, create a system of equations with which it is possible to solve for the water and land component T_Bs. Section 2 describes the data and sources that were used in our analysis and Section 3 details our deconvolution methodology. Section 4 describes the testing of our deconvolution method with simulated data and Section 5 shows validation of our results with *in situ* data.

2. DATA SOURCES

A multi-instrument data fusion algorithm such as this deconvolution technique requires numerous data sets to function and be properly validated. The water and vegetation fraction maps are derived from the Aqua and Terra MODIS observation products, MYD09A1 and MOD09A1 [10] respectively. These products consist of multiple, 2400x2400 pixel sinusoidal grid tiles with an approximately 500 m spatial resolution [11]. They are processed with the Vis/IR water and vegetation fraction algorithms specified in Section 3 then resampled on to a coarser 1 km scale MODIS sinusoidal grid in order to aid computational speed. The WindSat T_B data used in this paper [12, 13] was native-resolution swath data corrected for spillover effects and polarization rotation angles but not collocated between frequency channels. The data

---

Manuscript approved June 23, 2020.

set consisted of both horizontally and vertically polarized T_B observations from May 2014 through October 2017 from the area of interest over the Delmarva Peninsula. Additionally, satellite orbital position and pointing data from observations made on 3 June, 2014 was used to generate simulated T_Bs for testing purposes detailed in Sections 4 and 5.

Due to the mixed pixel effects which motivated this report, there has never been a network of long term soil moisture observing *in situ* sensors, designed for satellite retrieval validation, situated in a coastal region. Thus, to validate the deconvolved T_Bs from WindSat, we needed to gather such data. Accordingly, the Naval Research Laboratory (NRL) and United States Department of Agriculture Agricultural Research Service (USDA-ARS) collaborated to set up a soil moisture experiment in the Choptank region of the Delmarva Peninsula [14]. The site of this field campaign was specifically chosen because of the mix of open water and well characterized agricultural areas. Local soil types under the cropland are mostly a mix of poorly to moderately well-drained low-permeability sand. Land-use in this watershed is 58% agricultural, 33% forest, and only 9% urban usage. The most common crops are corn, soybean, and winter wheat double-cropped with soybeans.

Ten permanent sites were chosen within the Choptank watershed to sufficiently sample the area within a typical WindSat 10.7 GHz channel FOV. With cooperation from the area's farmers, instrumented stations were set up outside the field perimeters where they would not interfere with the crop planting or harvest over the course of several years. Each permanent station is equipped with four Stevens Hydra Probes [15] to measure soil moisture and soil temperature at depths of 5, 10, 20, and 50 cm, as well as additional instrumentation for gathering precipitation, solar radiation, and air temperature measurements. *In situ* measurements were recorded every hour. We used this data, in conjunction with a radiative transfer model (RTM), to produce land component brightness temperatures ($T_{B,\mathrm{Land}}$s) with which to validate the results of our deconvolution of WindSat T_B observations; this is documented in Section 5.

3. METHODOLOGY

The passive microwave deconvolution process detailed in this paper is done in three steps. In the first step, Vis/IR imagery from the MODIS spectrometers on board NASA's Aqua and Terra satellites is used to produce high resolution (1 km or smaller) maps of the fractional surface area coverage for open water (both fresh and saline). We also produce high resolution fractional area maps of the vegetation canopy for later use in our validation. In the second step, the antenna pattern for each feed horn, as projected on the Earth's surface, is used to apply relative gain weighting to these water coverage factions for each Vis/IR map pixel within the radiometer's FOV. This yields the relative mixing ratios for water and land T_B emissions for each WindSat observation. In the final step, these mixing ratios and the observed T_Bs from several adjacent WindSat observations are used to construct a system of linear equations. These systems of equations are then solved via least-squares minimization, yielding the deconvolved component T_Bs for water and land. The following subsections below explain each of these steps in greater detail.

In this report, we will frequently use terms that correspond to fractional area coverages and brightness temperatures on several different physical resolution scales and with different physical meanings. For clarity, we will consistently use the nomenclature described here. For fractional area coverages and brightness temperatures on a Vis/IR scale, 15 m through 1 km, we will use f_α and $\tau_{\mathrm{B},\tau}$ respectively. For antenna gain weighted fractional area coverages and brightness temperatures describing a microwave radiometer's FOV, we will correspondingly use F_α and $T_{B,\alpha}$. For both resolution scales, α specifies a component passive microwave emission source; e.g. *Water*, *Land*, *Soil*, or vegetation (*Vegt*); or the simulated or observed convolved values; e.g. *Sim* or *Obsv*. Additionally, when we perform a summation of numerous individual Vis/IR pixels we will index those values with the subscripts i or j and when referring to one of a set of passive microwave radiometer FOVs we will designate individual observations with a subscript m or n.

3.1 Water Fraction Estimation

Given the spatial footprint size of the WindSat radiometer's 10.7 and 18.7 GHz antenna gain patterns, a spatial resolution of 1 km for Vis/IR data was expected to provide sufficient localization for water coverage. This assumption was verified using simulated data; the results are detailed in Appendix A. Given the sufficiency of 1 km resolution and the need for large area coverage with a short revisit time, we chose to utilize 8-day composite surface reflectance (R) data from bands 1 (620-670 nm) and 2 (841-876 nm) acquired by both Aqua MODIS and Terra MODIS. Some cloud cover mitigation was required; therefore, we used a method developed by Miller et al. [16] to identify cloud cover by adding reactance values from bands 1 and 2 together and eliminating observations that satisfy $R_1 + R_2 > 0.65$.

We used a linear mixing model and decision tree approach from Sun et al. [17] to estimate fractional water coverage using MODIS reflectance observations. The difference in reflectance between bands 1 and 2 for the i^{th} MODIS pixel can be expressed as a function of its water fraction, $f_{\text{Water,i}}$, via

$$\Delta R_{\text{i}} = R_{2,\text{i}} - R_{1,\text{i}} \quad = \; f_{\text{Water,i}} \Delta R_{\text{Water}} + (1 - f_{\text{Water,i}})\, \Delta R_{\text{Land}} \tag{1}$$

Here, $\Delta R_{\text{Water}} = 0.0291$ and $\Delta R_{\text{Land}} = 0.0917$ are threshold reflectance values for pure water and land pixels. Pixels with reflectance values less than or equal to ΔR_{Water} are considered pure water, while pixels where ΔR_{Land} is less than or equal to ΔR_{i} are pure land, and those with values in between are mixed pixels. Thus, we can calculate the water fraction for the i^{th} MODIS pixel, $f_{\text{Water,i}}$, as a piecewise function

$$f_{Water,i} = \begin{Bmatrix} 1 & \Delta R_{\text{i}} \leq \Delta R_{\text{Water}} \\ \frac{\Delta R_{\text{Land}} - \Delta R_{\text{i}}}{\Delta R_{\text{Land}} - \Delta R_{\text{Water}}} & \Delta R_{\text{Water}} < \Delta R_{\text{i}} < \Delta R_{\text{Land}} \\ 0 & \Delta R_{\text{Land}} \leq \Delta R_{\text{i}} \end{Bmatrix} \tag{2}$$

Sun et al. evaluated this technique to have an error rate of ±4.4% when estimating the water coverage fraction for an individual MODIS pixel.

The final step in producing useful water fraction maps is to average the two maps produced from Aqua and Terra MODIS data and fill any remaining observation gaps caused by clouds or other anomalies. To do this, we construct composite 8-day maps in several steps. For each pixel in our composite maps, we first average the corresponding pixel from the Aqua and Terra based 8-day maps. If no data exists for that pixel in one map but it does in the other, then the value from the existing pixel is used in the composite. Next, we fill in any remaining empty pixels in the composite water map with the value from the previous 8-day composite water fraction map. Finally, should any pixels remain empty, they are filled with the average value of the four 250 m resolution subpixels from the static MODIS land/water mask (MOD44W) [18]. Figure 1 shows a sample plot of the composite water fraction map (left) from the Delmarva Peninsula.

3.2 Vegetation Fraction Estimation

In addition to the water fraction, the vegetation coverage fraction will be needed. Therefore, to determine the fractional area of the vegetation canopy for the i^{th} MODIS pixel ($f_{\text{Vegt,i}}$), we utilize an approach by Gitelson [19,20] which uses the Wide Dynamic Range Vegetative Index (WDRVI) [21] which is defined as

$$WDRVI_i = \frac{\gamma R_{1,i} - R_{2,i}}{\gamma R_{1,i} + R_{2,i}} \tag{3}$$

where $\gamma = 0.3$ and $R_{1,i}$ and $R_{2,i}$ are the reflectances from MODIS bands 1 and 2 respectively. As the name implies, the WDRVI maintains sensitivity at higher fractional vegetation coverage levels when compared to the more standard Normalized Difference Vegetation Index. Finally, we determine the fractional vegetation coverage using

$$f_{\mathrm{Vegt},i} = 80.838 * \mathrm{WDRVI}_i + 34.021 \tag{4}$$

where the linear parameters come from Gitelson [20]. This formula was developed in order to estimate the fractional vegetation coverage from MODIS observations for both maize and soybean fields simultaneously.

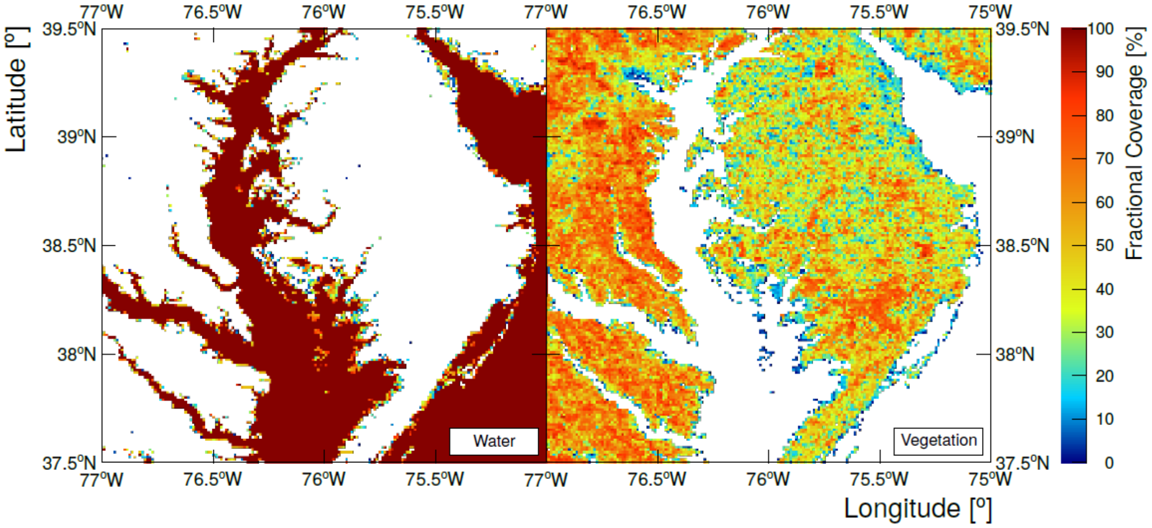

Fig. 1 – These plots show the 8-day composite water (left) and vegetation (right) fractional coverage maps over the Delmarva Peninsula on June 5, 2014.

Gaps in the resulting 8-day vegetation fraction maps from Aqua or Terra also need to be rectified by producing 8-day filled composite vegetation fraction maps. For each MODIS grid pixel in our area of interest, the corresponding composite water map is checked to determine if any land is present. If it is, then the composite vegetation map pixel is assigned a value that is the average of the Aqua and Terra vegetation map pixel values. If no data exists for a given pixel in one map but there is data in the other, the existing pixel data is used in the composite. Next, we fill missing pixels in the composite vegetation map by using the value from the previous 8-day composite map after adjusting the value by the average difference between the current and previous values from the eight surrounding pixels. Thus,

$$f_{Vegt,i} = f'_{Vegt,i}\left(1 + \sum_j \frac{f_{Vegt,j} - f'_{Vegt,j}}{f_{Vegt,j}}\right) \tag{5}$$

where the summation is over the eight surrounding pixels, if they exist, and a prime denotes a fractional value from the previous 8-day composite map. If the previous 8-day composite pixel is also empty, we would fill the empty pixel with the average of the current composite values from the eight surrounding pixels, provided more than four of those exist. Finally, should the pixel still be unfilled, we assign a standard value of 50% to it. Figure 1 also shows a plot of the composite vegetation fraction map (right) from the Delmarva Peninsula.

3.3 Antenna Pattern Weighting and Deconvolution

The radiometer observed brightness temperature ($T_{B,\mathrm{Obsv}}$) can be expressed as a linear combination of the brightness temperatures directly emitted from open water bodies ($T_{B,\mathrm{Water}}$) and land ($T_{B,\mathrm{Land}}$). Thus,

$$T_{B,\mathrm{Obsv}} = F_{\mathrm{Land}}\ T_{B,\mathrm{Land}} + F_{\mathrm{Water}}\ T_{B,\mathrm{Water}} \tag{6}$$

where for each type of emitting terrain, α, the weighting factor for that component type is

$$F_\alpha = \int f_\alpha(\Omega) G(\Omega) d\Omega \tag{7}$$

Here the spatial coverage function for each terrain type, $f_\alpha(\Omega)$, is weighted by the radiometer's antenna gain function, $G(\Omega)$, and integrated over the entire surface area of the radiometer's FOV. The weighting factor can be estimated with a simple sum of these weighted fractional coverages,

$$F_\alpha = \sum_i f_{\alpha,i} G_i \tag{8}$$

where we approximate the integration of a continuous spatial distribution as a summation over the set of fractional coverage estimates from the MODIS 1 km sinusoidal grid pixels within the radiometer observation's FOV. Here $f_{\alpha,\mathrm{i}}$ is weighted by the antenna gain relative to maximum received power, G_i, as computed for the geographic center of the i^{th} pixel and projected on the Earth's surface; additionally, we define $f_{\mathrm{Land,i}}$ to be the remainder when $f_{\mathrm{Water;i}}$ is subtracted from unity. After performing this operation for every passive microwave observation, we can proceed with an observation by observation deconvolution of the radiometer observed brightness temperatures ($T_{B,\mathrm{Obsv}}$s). For each passive microwave observation, we use Eq(6) to compute the residual between $T_{B,\mathrm{Obsv}}$ and a linear mixing of the $T_{B,\mathrm{Land}}$ and $T_{B,\mathrm{Water}}$ component brightness temperatures. Thus,

$$R_\mathrm{m} = [T_{B,\mathrm{Obsv,m}} - (F_{\mathrm{Land,m}} T_{B,\mathrm{Land}} + F_{\mathrm{Water,m}} T_{B,\mathrm{Water}})]^2 \tag{9}$$

where R_m is the residual term and $F_{\alpha,m}$ is the weighting term for terrain type α within the m^{th} radiometer observation. Assuming that $T_{B,\mathrm{Land}}$ and $T_{B,\mathrm{Water}}$ remain constant across the set of residuals computed from the m^{th} observation and its most spatially proximate neighbors, we can minimize the sum of these residuals and find the best fitting $T_{B,\mathrm{Land}}$ for the m^{th} passive microwave observation.

As a qualitative test, we applied our method to an area with a relatively simple coastline. Figure 2 shows an example of horizontally polarized 18.7 GHz T_Bs observed over the Florida peninsula by the WindSat radiometer before (left) and after (right) application of the deconvolution process. The deconvolution process removes the effect of mixed pixels containing both land and water along the coastline. Furthermore, Lake Okeechobee is not evident in the $T_{B,\mathrm{Land}}$ image, having been replaced with nominally correct looking land-based brightness temperature values. It does not, however, correct the T_B values for the Everglades region where we cannot readily distinguish between land and water due to overlying and floating vegetation. These effects are more starkly visible in Figure 3, which shows the bias values between the deconvolved $T_{B,\mathrm{Land}}$ values and their corresponding original $T_{B,\mathrm{Obsv}}$ values.

4. SIMULATED DATA TESTING

The first quantitative test of the effectiveness of our deconvolution approach was on artificial data simulated under ideal conditions using a Monte Carlo technique. The values in all our simulated maps and masks were randomly generated using a Mersenne Twister engine from the C++ standard library. Pixel values for topographic features, e.g. water presence, vegetation, surface temperatures, soil moisture, etc., were autocorrelated with themselves over a distance of 10 km. All of our simulated maps were square 2D arrays which we used as analogs for MODIS sinusoidal grid tiles. Additionally, the topographic features of all of these maps were contiguous across the map edges, allowing FOVs that spanned multiple MODIS grid tiles to run off the top/right map edges and continue onto the bottom/left edges and vice versa.

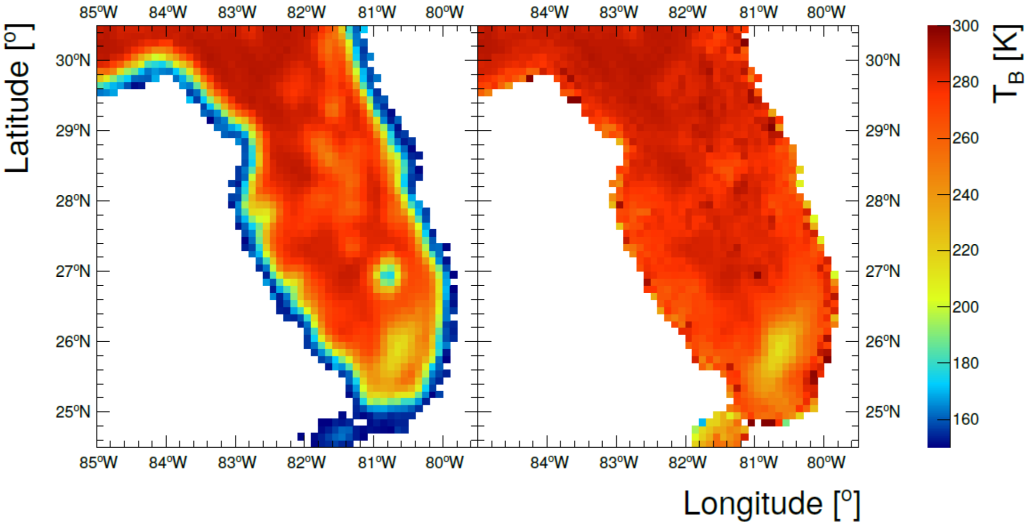

Fig. 2 – These plots show T_Bs for WindSat's horizontally polarized 18.7 GHz frequency channel over the Florida peninsula. The left plot shows T_Bs as observed, while the right plot shows the land component T_Bs derived after removing open water emissions using our deconvolution approach.

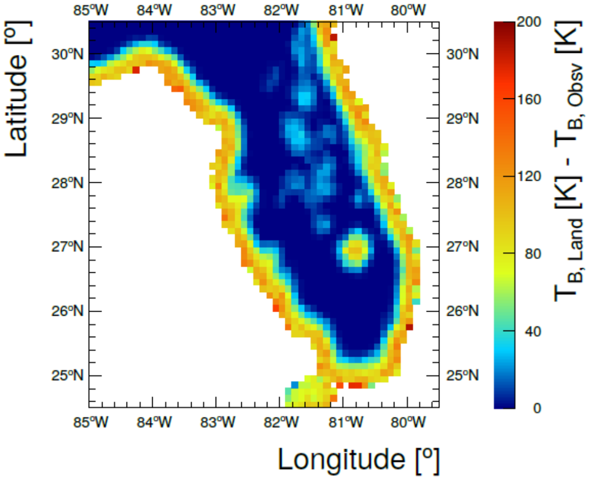

Fig. 3 – These plots show the difference between $T_{B,\text{Land}}$ and $T_{B,\text{Obsv}}$ for WindSat's horizontally polarized 18.7 GHz frequency channel over the Florida peninsula. Pixels without any land are left unfilled.

First, we produced twenty-five master land/water masks measuring 76800x76800 pixels which cover an area about 1200kmx1200km; this equates to a spatial resolution of approximately 15mx15m. These masks are *binary*, in that each pixel is either land or water; additionally, each mask has a differing ratio of total water to total land covered areas. Next, for each individual land/water mask, we also randomly generated a binary vegetation coverage for each land covered pixel; either a land pixel is vegetation covered or it is not. We then downscaled these master water and vegetation maps to a 1 km scale or 1200x1200 pixel grid.

The following analysis is the result of comparisons using simulated brightness temperatures for the WindSat radiometer's 10.7 GHz channel for both horizontal and vertical polarizations. For each pixel within each of the twenty-five maps, we generated physically realistic brightness temperatures (τ_Bs) using both a sea-based and a land-based radiative transfer model. We generated $\tau_{B,\text{Water}}$ values using a model, based on work by Meissner and Wentz [22,23,24], which produces T_Bs as a function of sea surface temperature and ocean wind speeds. We assumed these wind speeds to be a constant 10 m/s. To generate values for $\tau_{B,\text{Land}}$, we used the same Dobson semi-empirical mixing model [25,26] and coupled τ-ω vegetation canopy model [27,28] used in our land surface retrieval algorithm [29,30], which requires inputs for the land surface temperature (K), vegetative water content (kg/m^2), and soil moisture fraction (g/cm^3). We produced a $\tau_{B,\text{Land}}$ value for each land pixel by computing both a brightness temperature with ($\tau_{B,\text{Vegt}}$) and without ($\tau_{B,\text{Soil}}$) an overlying vegetation canopy. Then, for each pixel these two land based component T_Bs were mixed according to

$$\tau_{B,\text{Land},i} = f_{\text{Vegt},i}\ \tau_{B,\text{Vegt},i} + (1 - f_{\text{Vegt},i})\ \tau_{B,\text{Soil},i} \tag{10}$$

Finally, we produced artificially convolved brightness temperatures to simulate radiometer observations from these Vis/IR scale τ_Bs in two steps. First, we obtained realistic orbital look angles and geolocation data from actual WindSat observations. To do this, we collected the set of all 10.7 GHz T_B observations made on 3 June, 2014 with coordinates between a latitude of 33°N and 43°N and a longitude of 0°W and 180°W; this resulted in a set of approximately 225,000 observations. Next, for each of these observations, we computed a simulated convolved $T_{B,\text{Sim}}$ by combining $\tau_{B,\text{Water}}$ and $\tau_{B,\text{Land}}$ values for each simulated Vis/IR pixel within the FOV as computed from each respective observation's orbital characteristics. Thus, for the m_{th} radiometer observation in our set,

$$T_{B,Sim,m} = \frac{\sum_i (f_{Water,i}\tau_{B,Water,i} + (1 - f_{Water,i})\tau_{B,Land,i})G_{m,i}}{\sum_i G_{m,i}} \tag{11}$$

where the summation is over all simulated Vis/IR pixels within the m_{th} radiometer FOV characterized by the relative antenna gain factor for each Vis/IR pixel ($G_{m,i}$).

In performing our deconvolution, we require sufficient signal from both land and water to be successful; thus, the deconvolution algorithm is only executed when the observation of interest or at least one its neighbors satisfies the condition that $0.10 < F_{\text{Water},m} < 0.90$. We generated a $T_{B,\text{Sim}}$ value using each of the 225,000 WindSat observation FOVs applied to every one of the twenty-five simulated maps. The $F_{\text{Water},m}$ threshold condition results in a sample size of approximately 1.25 million $T_{B,\text{Sim}}$ values on which we could attempt deconvolution. Finally, we used the simulated Vis/IR water fraction maps to execute our deconvolution technique and separate the $T_{B,\text{Sim}}$ back into their component $T_{B,\text{Water}}$ and $T_{B,\text{Land}}$ values. This entire procedure is diagrammed in Figure 4.

By comparing the differences between the source $T_{B,\text{Land}}$ values produced by the RTM and the resulting deconvolved $T_{B,\text{Land}}$ values, we can ascertain the algorithm's effectiveness and accuracy as well as the magnitude of any noise introduced by the deconvolution process. Table 1 shows the number of samples, the Pearson correlation coefficient (R), bias, and root mean squared error (RMSE) values for this comparison for both polarizations from WindSat's 10.7 GHz frequency band. We also compared the RTM sourced $T_{B,\mathrm{Land}}$ values to the convolved $T_{B,\mathrm{Sim}}$ values to show the degree of water contamination that was removed. These comparisons are made using ten bins based on the computed F_{Water} value for the deconvolved $T_{B,\mathrm{Sim}}$; each bin spans a 5% F_{Water} range, yielding a sampling of FOVs with between 0% and 50% water contamination by signal contribution. The first bin, defined by the condition: $0\% < F_{\mathrm{Water}} < 5\%$, will be used as a control since it contains almost no water contamination but was still processed by the deconvolution algorithm.

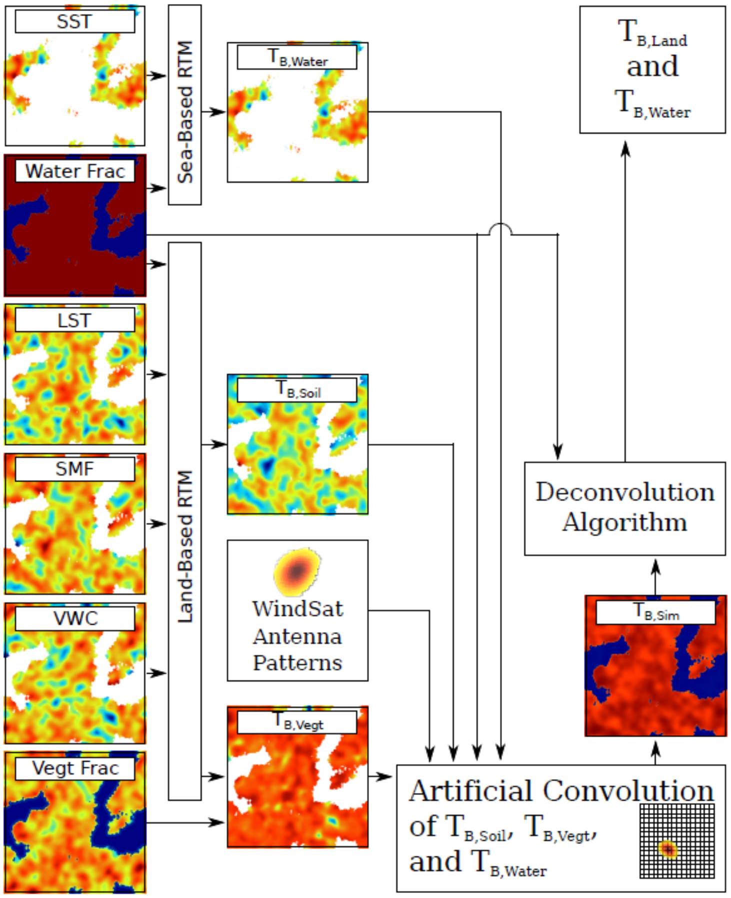

Fig. 4 – This diagram shows the procedure for testing the deconvolution algorithm via Monte Carlo generated data. Randomly generated values on a 1200_1200 grid for the sea surface temperature (SST), land surface temperature (LST), water and vegetation fractions, soil moisture fraction (SMF), and vegetative water content (VWC) are fed into land and sea based radiative transfer models to produce simulated land and water component brightness temperatures which are then artificially convolved into simulated radiometer observations, denoted as $T_{B,\mathrm{Sim}}$s. These $T_{B,\mathrm{Sim}}$s are then deconvolved back into component $T_{B,\mathrm{Land}}$ and $T_{B,\mathrm{Water}}$ values. These deconvolved values are subsequently compared to their corresponding source values from before their convolution.

We first note that both the $T_{B,\mathrm{Sim}}$ and $T_{B,\mathrm{Land}}$ R values are near unity in the control bin for both polarizations, indicating that the water present is having a small impact on the convolved T_Bs. However, even with that small amount of water signal, both the biases and RMSEs for both polarizations are smaller after the deconvolution process. The RMSE values after deconvolution are 1.8-2.6 K; this suggests that this is the noise floor introduced by the deconvolution process itself. While the biases for the $T_{B,\mathrm{Sim}}$ values are monotonically decreasing by significant values as the amount of water signal increases, the deconvolved $T_{B,\mathrm{Land}}$ bias values remain nearly constant. This provides clear proof that the deconvolution process is successfully removing the water signal contribution. Furthermore, the RMSE values for the deconvolved $T_{B,\mathrm{Land}}$ values gain only 2.5-3 K as F_{Water} values approach 50% contamination. This, in combination with the near zero bias values, indicates that error rates are both small, in comparison to the magnitude of the signal contribution being removed, and evenly distributed about the true land T_B values. Thus we can conclude that there is no significant systematic bias introduced by the deconvolution process.

5. *IN SITU* TESTING

We collected *in situ* soil moisture and related data on the Delmarva Peninsula during the spring, summer, and autumn seasons from 2014 through 2017and used it to test our deconvolution algorithm. We did this by using this data to produce, via the previously detailed RTM, simulated land component T_Bs from these measurements. First, we applied our deconvolution method to WindSat passive microwave observations to produce $T_{B,\mathrm{Land}}$ estimates for each observation made over the *in situ* sites for the 10.7 and 18.7 GHz frequency bands with both vertical and horizontal polarizations. Next, for each WindSat observation's FOV over the *in situ* network, we computed the averaged soil moisture fraction (SMF), soil temperature, and atmospheric temperature. *In situ* soil moisture data was collected from a depth of 5 cm. These averages, denoted by $\hat{X}_m$, are computed according to

$$\hat{X}_m = \frac{\sum_i x_i G_{m,i}}{\sum_i G_{m,i}} \tag{12}$$

where $G_{\mathrm{m,i}}$ is the antenna gain for the i^{th} *in situ* site within the m_{th} observation's FOV and x_i is the local SMF, soil temperature, or atmospheric temperature value at that site. Finally, using these averages for each WindSat observation's FOV over the *in situ* site, we estimated the observable $T_{B,\mathrm{Land}}$ value at the top of the atmosphere via the land based surface radiative transfer model in the previous section. There were about 500 samples per analysis bin at 10 GHz and about 600 at 18 GHz.

For each day with a WindSat overflight, we then selected one observation to analyze for each of six analysis bins. These bins are divided according to the observations' F_{Water} value, like in the previous section, but here the maximum F_{Water} value is 30%. We will once again treat the 0-5% bin as our control. Figure 5 shows the locations of the ten *in situ* network sites and the -3 dB contours of the selected WindSat observations for June 5, 2014.

Our RTM modeling differs slightly for this analysis from the one we used with simulated data. Here, we used the MODIS derived vegetation fraction estimates detailed in Section 2 to perform the soil and vegetation mixing. Additionally, whereas the soil and vegetation canopy had the same physical temperature in our simulated data testing, here we used the averaged *in situ* soil temperature for the $T_{B,\mathrm{Soil}}$ RTM estimates and the averaged *in situ* air temperature for the canopy temperature in our τ-ω attenuation estimates. Vegetative water content (VWC) values were assumed to be a constant 0.67 kg/m^2 this value is both physically reasonable for the agricultural products in the region and minimizes the biases between RTM predictions and observed T_B values. We did not vary this parameter to account for seasonal variations in VWC, nor did account for VWC variations for different crop types and their relative weighting within our FOVs.

Table 1: Pearson correlation coefficient (R), bias, and root mean squared error (RMSE values for deconvolved, $T_{B,\text{Land}}$, and convolved, $T_{B,\text{Sim}}$, simulated brightness temperatures compared to simulated land component T_B source values. Comparisons were made for T_Bs simulating both vertical and horizontal polarizations in WindSat's 10 GHz frequency band and were binned according to each observation's antenna gain pattern weighted water fraction value (F_{Water}).

Channel		# Samples	R		Bias [K]		RMSE [K]		F_{water}
			$T_{B,\text{Sim}}$	$T_{B,\text{Land}}$	$T_{B,\text{Sim}}$	$T_{B,\text{Land}}$	$T_{B,\text{Sim}}$	$T_{B,\text{Land}}$	
10 GHz	V-Pol	102,654	0.944	0.953	−2.748	−0.294	3.399	1.858	0–5%
		109,867	0.920	0.923	−6.939	−0.254	7.347	2.426	5–10%
		80,479	0.911	0.898	−11.870	−0.185	12.140	2.887	10–15%
		65,864	0.911	0.882	−16.725	−0.215	16.923	3.201	15–20%
		57,240	0.912	0.871	−21.521	−0.193	21.681	3.418	20–25%
		51,681	0.913	0.868	−26.281	−0.122	26.423	3.529	25–30%
		48,284	0.909	0.858	−31.083	−0.119	31.219	3.762	30–35%
		45,643	0.906	0.850	−35.878	−0.131	36.013	3.943	35–40%
		44,008	0.896	0.842	−40.710	−0.103	40.852	4.129	40–45%
		43,375	0.885	0.834	−45.507	−0.167	45.656	4.265	45–50%
	H-Pol	102,654	0.893	0.918	−4.110	−0.334	5.079	2.597	0–5%
		109,867	0.854	0.879	−10.377	−0.265	10.977	3.260	5–10%
		80,479	0.839	0.840	−17.752	−0.245	18.139	3.946	10–15%
		65,864	0.840	0.815	−25.013	−0.308	25.283	4.427	15–20%
		57,240	0.841	0.800	−32.185	−0.290	32.390	4.753	20–25%
		51,681	0.842	0.794	−39.313	−0.197	39.480	4.935	25–30%
		48,284	0.837	0.781	−46.492	−0.193	46.641	5.240	30–35%
		45,643	0.833	0.771	−53.676	−0.217	53.813	5.496	35–40%
		44,008	0.819	0.760	−60.882	−0.172	61.019	5.776	40–45%
		43,375	0.803	0.749	−68.062	−0.241	68.200	5.953	45–50%

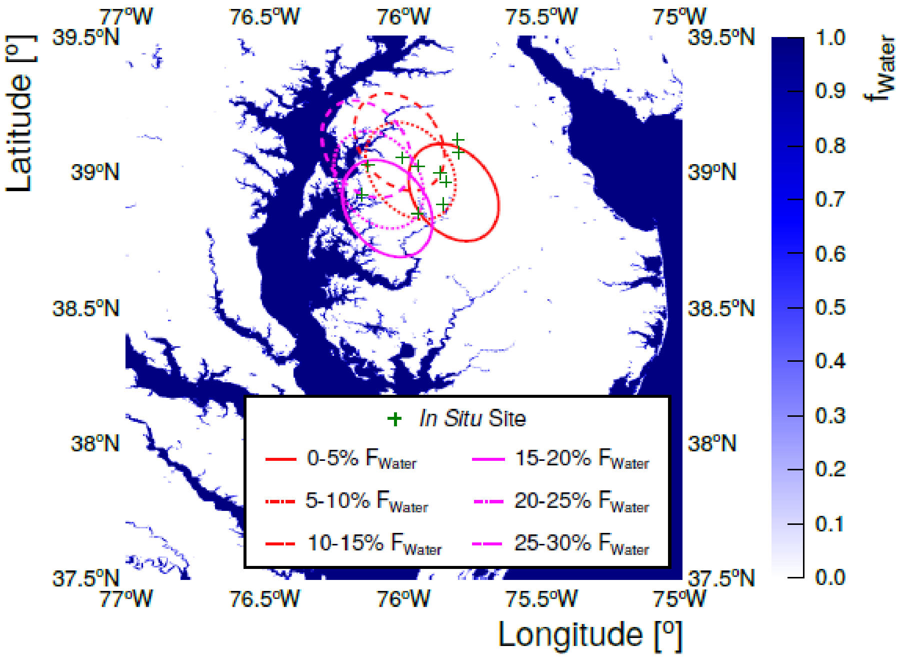

Fig. 5 – This plot shows the Vis/IR water fraction on June 5, 2014. It also shows the geographic locations of all ten *in situ* network sites and the -3 dB contour for WindSat's 10.7 GHz FOV for each of the six analysis bins. Each FOV represents the observation from that F_{Water} bin that is geographically closest to the center of the *in situ* network.

Figures 6 and 7 show correlation plots of the convolved T_B values modeled from *in situ* observations versus the deconvolved $T_{B,Land}$ values and also versus the original observed WindSat $T_{B,Obsv}$ values from the 10.7 and 18.7 GHz frequency bands respectively. Furthermore, the R, bias, and RMSE values for these plots are contained in Table 2.

At this point we wish to address the strengths and weaknesses of comparing RTM T_B values generated from *in situ* data to passive microwave radiometer observed T_Bs T_Bs. First, regardless of how extensive the sampling sites within the *in situ* network, they are point sources; whereas passive microwave radiometers observe an integrated two-dimensional surface area. Looking at the correlation coefficients for our control bins for both 10 and 18 GHz we see a very strong correlation between the *in situ* data derived T_B values and both radiometer derived T_B values. This argues in strongly favor of the reasonableness of this comparison. However, it should be noted that we are comparing a fixed network on the ground to radiometer FOVs that cover different areas. Indeed, as we look for increasingly water contaminated T_B observations, the average distance between the geographic center of our *in situ* network and the center of the radiometer FOV increases. Thus, we excluded analysis of FOVs with an F_{Water} value greater than 30%, as this average distance exceeded the size of a typical WindSat 10 GHz footprint. This effect unfortunately means that any degradation we see in the correlation between the *in situ* and radiometer derived T_Bs will be a function of both the increased distance and the amount of water contamination. While it is impossible to separate out this increased distance effect, the relative performance between the original, water contaminated T_B values and the deconvolved, land component T_B values makes a strong qualitative case for the success of our technique.

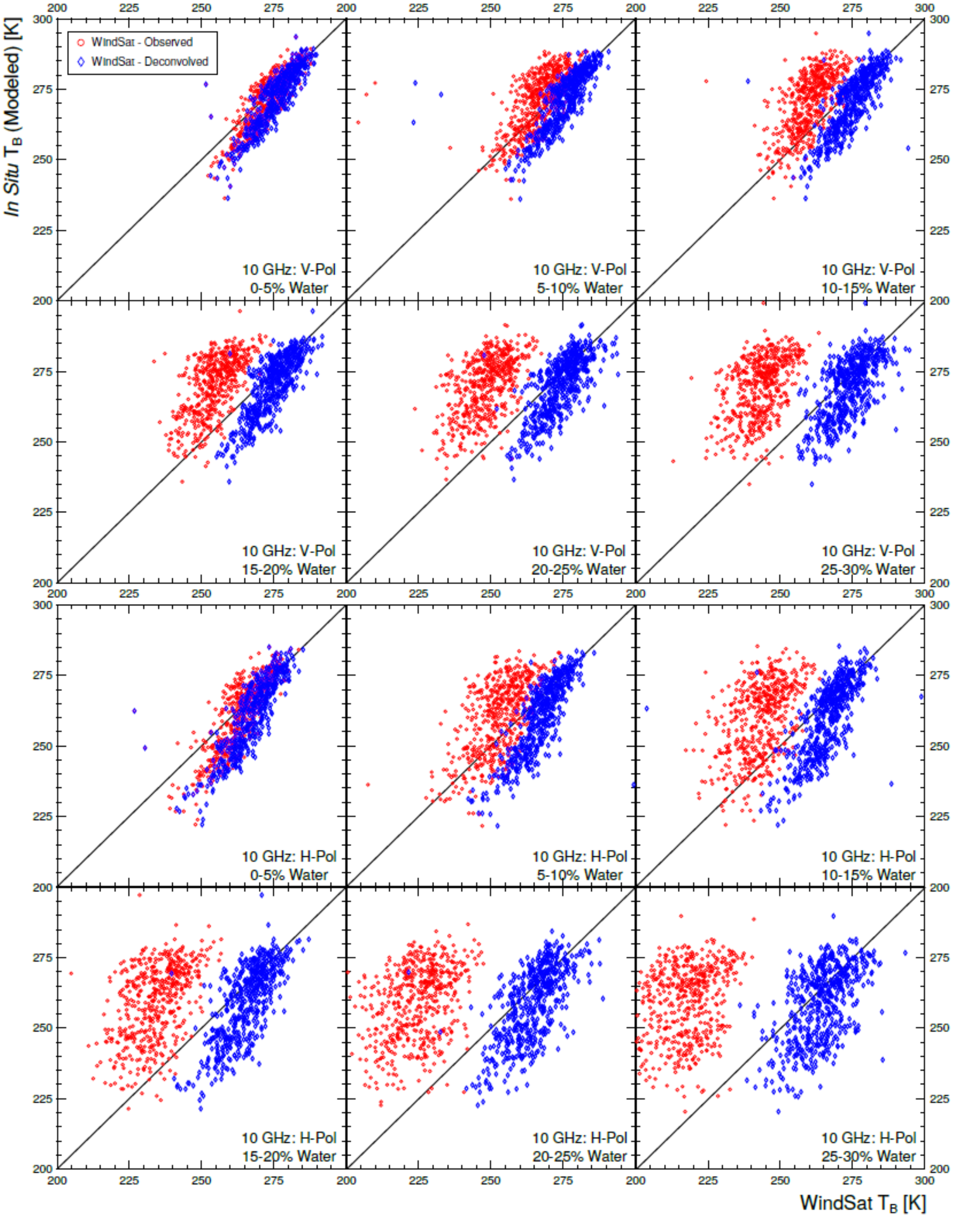

Fig. 6 – Correlation plots for the 10 GHz vertically (top two rows) and horizontally (bottom two rows) polarized *in situ* modeled T_B values versus the original observed WindSat T_B values (red circles) and the deconvolved land component T_B values (blue diamonds). Samples are binned according to the antenna pattern weighted water fraction value (F_{Water}) for each observation's FOV.

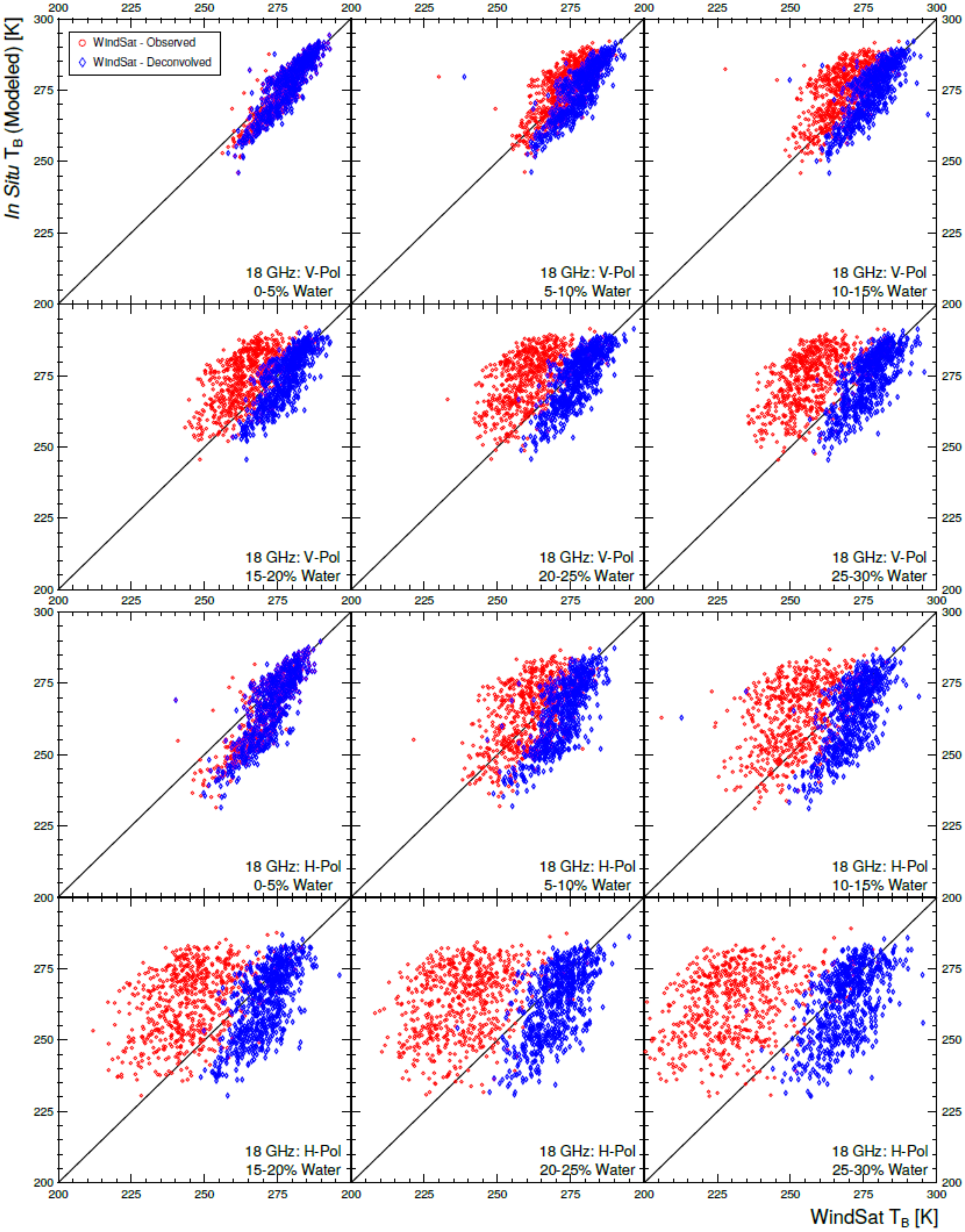

Fig. 7 – Correlation plots for the 18 GHz vertically (top two rows) and horizontally (bottom two rows) polarized *in situ* modeled T_B values versus the original observed WindSat T_B values (red circles) and the deconvolved land component T_B values (blue diamonds). Samples are binned according to the antenna pattern weighted water fraction value (F_{Water}) for each observation's FOV.

Looking at Figures 6 and 7, we see that both deconvolved and observed distributions start tight to the 1:1 correlation line in the control bins. However, while the deconvolved distributions stay on the 1:1 correlation line the observed distribution steadily diverges from it with increasing F_{Water} values. This is obvious when looking at the bias values in Table 2, which are monotonically decreasing for observed WindSat T_B values with increasing F_{Water}. T_B*s* emitted from water are significantly lower than those produced by land, even at the same physical temperature; thus, the larger the emission contribution from water within the convolved T_B observation, the lower the T_B value. In contrast to this, the bias values for the deconvolved T_B values remain virtually constant; strongly indicating the successful removal of the passive microwave signal from water. Furthermore, the plots show both distributions in both frequency bands expanding in width. However, this increasing magnitude of average error is far more prominent in the observed T_B distributions. Once again, it is produced by the combination of the degree of water contamination in the signal and the average geographic distance between the *in situ* sites and the WindSat FOV. The deconvolved T_B*s* better performance in average error magnitude is borne out by inspecting the RMSE values for the two distributions.

Additionally, we have also included a figure σ(Error), in Table 2 intended to directly measure this effect. This σ (Error) column is the standard deviation of the difference between the *in situ* T_B values and the original and deconvolved T_B values. Inspecting these standard deviations we see that for every $\mathrm{F}_{\mathrm{Water}}$ bin in both polarizations and both frequency bands, except the 0-5% bins in the 18 GHz band, the deconvolved T_B values always have smaller σ (Error) values. Furthermore, while both observed and deconvolved distributions have generally increasing σ (Error) values (indicative of increasing physical distance between samples) the deconvolved $T_{B,\mathrm{Land}}$ σ (Error) values increase far slower with increasing F_{Water} (indicative of less error in general). That, once again, indicates that the deconvolution algorithm is removing at least some part of the water contamination. These trends are also reflected in the RMSE values, which contain a mixture of the bias and σ (Error) signals we have already discussed.

6. DISCUSSION

Both our *in situ* based and Monte Carlo based analyses provide strong process in removing the water component from the observed T_B*s* in cases of mixed land and water passive microwave radiometer FOVs. Our best estimates for the additional noise introduced by the technique itself, 1.8-2.6 K, come from the control bins of our Monte Carlo analysis. Under the ideal circumstances presented by the Monte Carlo simulated data, our deconvolution algorithm removed nearly all water contamination signal from both 10.7 GHz channels while keeping the RMSE under 5 K for F_{Water} values of up to 30%. This would certainly indicate a potential to undertake soil moisture retrievals nearly up to the coastline if this technique is used.

The results provided by our *in situ* analysis are less promising, but they are also entangled in geographic colocation problems that confuse our results. Still, we can confidently say that the *in situ* analysis shows that at least some component of the water signal contamination is being removed successfully by the deconvolution process. Additionally, the bias and RMSE values remain high in the *in situ* 10 GHz and 18 GHz control bins. When looking at the slope of the distributions the reason becomes apparent. Our RTM T_B values display a larger dynamic range than the corresponding radiometer observed T_B*s*. Thus, our distributions, which start on the 1:1 correlation line at high T_B values stray from the line as the observed T_B value falls. This trend is also apparent, though less obvious, in every other F_{Water} bin. This shortcoming in our RTM modeling unfortunately introduces a systematic error into our analysis which raises the bias and RMSE values and partially obscures the results we are seeking. However, despite this effect RMSE values remain below 10 K for vertically polarized channels and below 13 K in the horizontally polarized channels. We can therefore argue that, absent this effect, the deconvolution algorithm should produce deconvolved land component T_Bs with even better bias and RMSE values.

Table 2 – Pearson correlation coefficient (R), bias, and root mean squared error (RMSE) values for the deconvolved land component T_B values ($T_{B,\text{Land}}$) and the original observed T_B values ($T_{B,\text{Obsv}}$) compared to land component T_B values generated from *in situ* data via NRL's land retrieval algorithm forward radiative transfer model. Comparisons were made for T_Bs simulating both vertical and horizontal polarizations in WindSat's 10.7 and 18.7 GHz frequency bands and are broken up into six bins depending on each observation's antenna gain pattern weighted water fraction value (F_{Water}). The average distance between the center of the samples' FOVs and the geographic center of the *in situ* network ($\overline{D}$) is also displayed.

Channel		$\bar{D}$ [km]	R		Bias [K]		RMSE [K]		σ(Error) [K]		F_{Water}
			$T_{B,\text{Obsv}}$	$T_{B,\text{Land}}$	$T_{B,\text{Obsv}}$	$T_{B,\text{Land}}$	$T_{B,\text{Obsv}}$	$T_{B,\text{Land}}$	$T_{B,\text{Obsv}}$	$T_{B,\text{Land}}$	
10 GHz	V-Pol	5.848	0.870	0.886	1.293	3.724	5.412	6.325	5.255	5.112	0–5%
		8.116	0.620	0.731	−5.213	4.108	9.830	8.195	8.333	7.091	5–10%
		12.796	0.637	0.786	−10.419	4.445	13.146	7.924	8.016	6.560	10–15%
		16.975	0.620	0.721	−15.768	4.669	17.821	8.691	8.303	7.330	15–20%
		20.696	0.540	0.647	−21.732	4.365	23.506	9.119	8.958	8.006	20–25%
		22.664	0.483	0.611	−26.433	4.354	28.107	9.554	9.555	8.504	25–30%
	H-Pol	5.848	0.828	0.847	2.241	6.274	7.899	9.742	7.575	7.453	0–5%
		8.116	0.494	0.657	−8.178	6.416	14.714	11.826	12.232	9.934	5–10%
		12.796	0.460	0.704	−16.552	6.570	20.364	11.464	11.864	9.394	10–15%
		16.975	0.465	0.637	−25.179	6.498	27.889	12.113	11.992	10.222	15–20%
		20.696	0.369	0.564	−34.571	5.748	36.933	12.339	12.994	10.919	20–25%
		22.664	0.287	0.505	−41.870	5.550	44.121	12.943	13.914	11.692	25–30%
18 GHz	V-Pol	4.136	0.903	0.892	1.305	1.960	4.181	4.698	3.972	4.270	0–5%
		10.506	0.738	0.830	−3.077	2.930	6.724	5.773	5.979	4.974	5–10%
		14.738	0.631	0.790	−6.777	3.087	9.970	6.420	7.313	5.629	10–15%
		17.756	0.626	0.724	−10.153	3.226	12.631	7.106	7.514	6.332	15–20%
		20.255	0.562	0.770	−13.416	3.183	15.829	6.793	8.400	6.001	20–25%
		21.852	0.545	0.712	−17.106	2.979	19.295	7.365	8.926	6.736	25–30%
	H-Pol	4.136	0.860	0.831	4.919	6.307	7.956	9.419	6.253	6.996	0–5%
		10.506	0.536	0.707	−4.250	7.365	11.163	11.015	10.322	8.190	5–10%
		14.738	0.415	0.639	−11.800	7.267	17.123	11.663	12.408	9.122	10–15%
		17.756	0.425	0.645	−18.543	6.955	22.500	11.490	12.744	9.146	15–20%
		20.255	0.340	0.605	−25.020	6.675	28.802	11.787	14.268	9.715	20–25%
		21.852	0.348	0.558	−32.120	6.018	35.502	12.040	15.124	10.428	25–30%

7. CONCLUSIONS

This report describes our technique to extend satellite based passive microwave observations into geographic regions previously excluded from reliable soil moisture retrievals through the development of a deconvolution algorithm for microwave radiometer T_B observations. Our approach separates passive microwave emissions from land and water based on surface information from Vis/IR data resulting in significantly improved agreement between deconvolved WindSat observations and modeled T_Bs based on *in situ* soil moisture measurements in coastal areas. Although we were not able to provide a direct comparison between our deconvolved land component T_Bs and directly observed land T_Bs, e.g. those gathered from an airborne passive microwave radiometer, we did present strong evidence that our technique could prove useful in future passive microwave satellite radiometer T_B retrievals in coastal areas. We hope that this provides the impetus for future exploration and further validation of this technique. Indeed, we believe that passive microwave component deconvolution could become a powerful tool for enhancing satellite based passive microwave environmental retrievals, including extending accurate soil moisture retrievals to coastal areas that are not currently reliably observed.

8. APPENDIX – SPATIAL RESOLUTION

This appendix details how we determined that 1 km resolution is a sufficient spatial resolution for the Vis/IR derived water fraction data used in our deconvolution method. In order to determine the necessary resolution for the Vis/IR derived water fraction data used in our deconvolution method, we need to investigate two related effects. The first is, "How much does a coarser sampling impact the accuracy of the approximation of a continuous integral by a discreet summation that we made in Eq(8)?" The second is, "How do errors in the accuracy of our water fraction estimation, introduced via coarsening spatial resolution of Vis/IR observation, affect the accuracy of our deconvolution?"

To answer the first question, we started with the twenty-five 15 m resolution binary land/water and vegetation masks we discussed in Section 4. For each master mask, we created a corresponding 30, 250, 500, and 1000 m resolution water fraction map by assigning each 15 m water covered binary pixel a value of 100 and each land covered binary pixel a value of 0 then averaging 2x2, 16x16, 32x32, and 64x64 blocks of pixels respectively and assigning the average value to the corresponding downscaled pixel. Next, we computed convolved $T_{B,\text{Sim}}$ values for our 225,000 WindSat observations using each of the 15 m maps and Eq(11). In order to eliminate noise from the deconvolution technique itself, we used constant but physically realistic values of $\tau_{B,\text{Water}}$ = 93.62 K for each binary water covered pixel and $\tau_{B,\text{Water}}$ = 236.46 K for each land covered pixel. We then used each of the corresponding lower resolution maps as the Vis/IR water fraction data source in the deconvolution algorithm and attempted to recover the fixed $T_{B,\text{Land}}$ and $T_{B,\text{Water}}$ values at each resolution. A block diagram of this process is illustrated in Figure A.8. The resulting component T_Bs were then compared to the fixed $\tau_{B,\text{Water}}$ and $\tau_{B,\text{Water}}$ values respectively. This resulted in both biases and RMSEs of less than 0.10 K for all resolutions. Thus, the summation approximation is valid even at Vis/IR spatial scales of 1 km. Given the aforementioned expected error rate for water fraction estimation is 4.4% and this analysis, we concluded that using a 1 km spatial resolution scale for our Vis/IR data products was the best option, as it reduced our computing resource requirements and would have little effect on the deconvolution accuracy.

To answer the second question, we looked to the worst case error scenario for water fraction estimation. To simulate the case in which we can only grossly estimate a Vis/IR pixel as all land or all water, we again deconvolved the $T_{B,\text{Sim}}$s generated using the 15 m master land/water masks. However, this time we used binary maps in which, at each resolution, we rounded each pixel either up to a 100% or down to a 0% water fraction value depending on whether the average value was greater or less than 50%. Table A.3 shows the biases and RMSEs for the resulting $T_{B,\text{Land}}$ and $T_{B,\text{Water}}$ values when compared to the static $\tau_{B,\text{Water}}$ and $\tau_{B,\text{Water}}$ values. Biases for $T_{B,\text{Water}}$ and $T_{B,\text{Land}}$ raise steadily as spatial resolution gets coarser. The same is true for RMSE values, with the exception of the 30 m resolution masks, which produced anomalously high RMSE values. This can probably be explained by the fact that at 30 m resolutions there are quite a few mixed pixels in any given FOV, while the higher resolution 250 m masks have fewer mixed pixels introducing errors. The 1 km masks have the fewest mixed pixels, but the errors from said pixels introduce correspondingly larger errors.

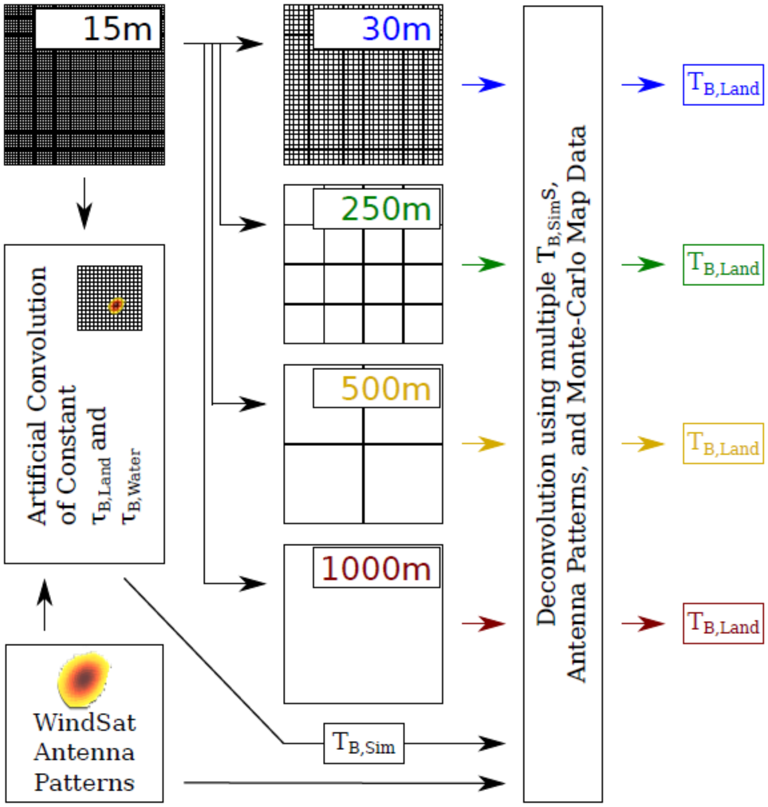

Fig. 8 –This diagram shows the procedure for testing the spatial resolution required for water fraction data. Master water masks (15 m resolution) are used to generate spatially downgraded 30, 250, 500, and 1000 m water masks. The 15 m masks are then used to artificially convolve simulated observable T_B values ($T_{B,\text{Sim}}$s) and the downgraded masks are subsequently used to deconvolve them back into land component T_B values ($T_{B,\text{Land}}$s).

Table 3 – T_B bias and root mean squared error values for different spatial resolutions of binary water masks used in deconvolution algorithm when compared to simulated 15 m resolution truth data.

	$T_{B,\text{Water}}$ [K]		$T_{B,\text{Land}}$ [K]	
Resolution [m]	Bias	RMSE	Bias	RMSE
30	-0.800	5.873	-1.983	7.270
250	-0.145	3.729	0.569	3.836
500	0.456	7.579	0.610	4.433
1000	0.758	8.549	0.694	5.895

ACKNOWLEDGMENTS

The MODIS Land Surface Reflectance (MOD09A1/MYD09A1) data products were retrieved from the online Data Pool, courtesy of the NASA Land Processes Distributed Active Archive Center (LP DAAC),

USGS/Earth Resources Observation and Science (EROS) Center, Sioux Falls, South Dakota, https://lpdaac.usgs.gov/data access/data pool.

REFERENCES

1. Y. Kerr, P. Waldteufel, J.-P. Wigneron, J. Martinuzzi, J. Font, M. Berger, “Soil moisture retrieval from space: the soil moisture and ocean salinity (SMOS) mission”, Geoscience and Remote Sensing, IEEE Transactions on 39 (2001) 1729-1735. doi:10.1109/36.942551.

2. D. Entekhabi, E. G. Njoku, P. E. O'Neill, K. H. Kellogg, W. T. Crow, W. N. Edelstein, J. K. Entin, S. D. Goodman, T. J. Jackson, J. Johnson, J. Kimball, J. R. Piepmeier, R. D. Koster, N. Martin, K. C. McDonald, M. Moghaddam, S. Moran, R. Reichle, J. C. Shi, M. W. Spencer, S. W. Thurman, L. Tsang, J. V. Zyl, “The soil moisture active passive (SMAP) mission”, Proceedings of the IEEE 98 (2010) 704-716. doi:10.1109/JPROC.2010.2043918.
3. T. Kawanishi, T. Sezai, Y. Ito, K. Imaoka, T. Takeshima, Y. Ishido, A. Shibata, M. Miura, H. Inahata, R. Spencer, “The advanced microwave scanning radiometer for the earth observing system (AMSR-E), NASDA's contribution to the EOS for global energy and water cycle studies”, IEEE Transactions on Geoscience and Remote Sensing 41 (2003) 184-194. doi:10.1109/TGRS.2002.808331.
4. P. Gaiser, K. St Germain, E. Twarog, G. Poe, W. Purdy, D. Richardson, W. Grossman, W. Jones, D. Spencer, G. Golba, J. Cleveland, L. Choy, R. Bevilacqua, P. Chang, “The WindSat spaceborne polarimetric microwave radiometer: sensor description and early orbit performance”, IEEE Transactions on Geoscience and Remote Sensing 42 (2004) 2347-2361. doi:10.1109/TGRS.2004.836867.
5. T. Bellerby, M. Taberner, A.Wilmshurst, M. Beaumont, E. Barrett, J. Scott, C. Durbin, “Retrieval of land and sea brightness temperatures from mixed coastal pixels in passive microwave data”, IEEE Transactions on Geoscience and Remote Sensing 36 (1998) 1844-1851. doi:10.1109/36.729355.

6. S. Limaye, W. L. Crosson, C. A. Laymon, E. G. Njoku, “Land cover-based optimal deconvolution of PALS L-band microwave brightness temperatures”, Remote Sensing of Environment 92 (2004) 497-506. URL: http://www.sciencedirect.com/science/article/pii/S0034425704001865. doi:http://dx.doi.org/10.1016/j.rse.2004.02.019, 2002 Soil Moisture Experiment (SMEX02).

7. Yanovsky, A. Tanner, B. Lambrigtsen, “Efficient deconvolution and spatial resolution enhancement from continuous and oversampled observations in microwave imagery”, in: 2014 13th Specialist Meeting on Microwave Radiometry and Remote Sensing of the Environment (MicroRad), 2014, pp.151-156. doi:10.1109/MicroRad.2014.6878929.

8. S. Limaye, W. L. Crosson, C. A. Laymon, “Estimating accuracy in optimal deconvolution of synthetic AMSR-E observations”, Remote Sensing of Environment 100 (2006) 133-142. URL: http://www.sciencedirect.com/science/article/pii/S0034425705003494. doi:https://doi.org/10.1016/j.rse.2005.10.008.

9. O. Justice, E. Vermote, J. R. G. Townshend, R. Defries, D. P. Roy, D. K. Hall, V. V. Salomonson, J. L. Privette, G. Riggs, A. Strahler, W. Lucht, R. B. Myneni, Y. Knyazikhin, S.W.

Running, R. R. Nemani, Z.Wan, A. R.Huete, W. van Leeuwen, R. E. Wolfe, L. Giglio, J. Muller, P. Lewis, M. J. Barnsley, "The moderate resolution imaging spectroradiometer (modis): land remote sensing for global change research", IEEE Transactions on Geoscience and Remote Sensing 36 (1998) 1228-1249. doi:10.1109/36.701075.

10. E. F. Vermote, S. Y. Kotchenova, J. P. Ray, MODIS Surface Reflectance Users Guide, Technical Report, MODIS Land Surface Reflectance Science Computing Facility, 2011.

11. L. Boschetti, D. Roy, A. A. Ho_mann, M. Humber, MODIS Collection 5.1 Burned Area Product - MCD45 Users Guide, Technical Report, MODISScience Team, 2013.

12. P. Gaiser, WindSat temperature data record, 2015a.

13. P. Gaiser, WindSat intermediate data record, 2015b.

14. E. M. Twarog, L. Li, P. W. Gaiser, E. R. Hunt, M. J. Cosh, "Eastern shore soil moisture experiment testbed and analysis, 2016. Unpublished.

15. K. Bellingham, Comprehensive Stevens Hydra Probe User's Manual, Technical Report, Stevens Water Monitoring Systems, Inc., 2015.

16. S. D. Miller, T. F. Lee, R. L. Fennimore, "Satellite-based imagery techniques for daytime cloud/snow delineation from MODIS", Journal of Applied Meteorology 44 (2005) 987-997. URL:https://doi.org/10.1175/JAM2252.1. doi:10.1175/JAM2252.1. arXiv:https://doi.org/10.1175/JAM2252.1.

17. Sun, Y. Yu, M. D. Goldberg, "Deriving water fraction and flood maps from modis images using a decision tree approach", IEEE Journal of Selected Topics in Applied Earth Observations and Remote Sensing 4 (2011) 814-825. doi:10.1109/JSTARS.2011.2125778.

18. M. Carroll, C. DiMiceli, J. Townshend, P. Noojipady, R. Sohlberg, Global 250 meter Land Water Mask User Guide, Technical Report, University of Maryland, 2009.

19. A. Via, A. A. Gitelson, "New developments in the remote estimation of the fraction of absorbed photosynthetically active radiation in crops", Geophysical Research Letters 32 (2005) n/a{n/a. URL: http://dx.doi.org/10.1029/2005GL023647.doi:10.1029/2005GL023647, l17403.

20. A. A. Gitelson, "Remote estimation of crop fractional vegetation cover: the use of noise equivalent as an indicator of performance of vegetation indices", International Journal of Remote Sensing 34 (2013) 6054-6066. URL: http://dx.doi.org/10.1080/01431161.2013.793868. doi:10.1080/01431161.2013.793868. arXiv:http://dx.doi.org/10.1080/01431161.2013.793868.

21. A. A. Gitelson, "Wide dynamic range vegetation index for remote quantification of biophysical characteristics of vegetation", Journal of Plant Physiology 161 (2004) 165-173. doi:http://dx.doi.org/10.1078/0176-1617-01176.

22. T. Meissner, F. J. Wentz, "The complex dielectric constant of pure and sea water from microwave satellite observations", IEEE Transactions on Geoscience and Remote Sensing 42 (2004) 183-1849. doi:10.1109/TGRS.2004.831888.

23. J. Wentz, “A model function for ocean microwave brightness temperatures”, Journal of Geophysical Research: Oceans 88 (1983) 1892-1908. URL:http://dx.doi.org/10.1029/JC088iC03p01892. doi:10.1029/JC088iC03p01892.

24. J. Wentz, “A two-scale scattering model for foam-free sea microwave brightness temperatures”, Journal of Geophysical Research 80 (1975) 3441-3446. URL:http://dx.doi.org/10.1029/JC080i024p03441. doi:10.1029/JC080i024p03441.

25. M. C. Dobson, F. T. Ulaby, M. T. Hallikainen, M. A. El-rayes, “Microwave dielectric behavior of wet soil-part II: Dielectric mixing models”, IEEE Transactions on Geoscience and Remote Sensing GE-23 (1985) 35-46. doi:10.1109/TGRS.1985.289498.
26. N. R. Peplinski, F. T. Ulaby, M. C. Dobson, Dielectric properties of soils in the 0.3-1.3-ghz range, IEEE Transactions on Geoscience and Remote Sensing 33 (1995) 803-807. doi:10.1109/36.387598.

27. T. J. Jackson, T. J. Schmugge, J. R. Wang,” Passive microwave sensing of soil moisture under vegetation canopies”, Water Resources Research 18 (1982) 1137-1142. URL: http://dx.doi.org/10.1029/WR018i004p01137. doi:10.1029/WR018i004p01137.

28. P. ONeill, S. Chan, E. Njoku, T. Jackson, R. Bindlish, “SMAP - Algorithm Theoretical Basis Document - Level 2 & 3 Soil Moisture (Passive) Data Products”, Technical Report, Jet Propulsion Laboratory, 2012.

29. L. Li, P. Gaiser, B. Gao, R. Bevilacqua, T. Jackson, E. Njoku, C. Rudiger, J. Calvet, R. Bindlish, “WindSat global soil moisture retrieval and validation”, IEEE Transactions on Geoscience and Remote Sensing 48 (2010) 2224-2241.

30. E. G. Njoku, L. Li, “Retrieval of land surface parameters using passive microwave measurements at 6-18 GHz”, IEEE Transactions on Geoscience and Remote Sensing 37 (1999) 79-93. doi:10.1109/36.739125.